Post-event Analysis of the 9 February 2024 X-Flare

Erik Schmölter and Jens Berdermann

Abstract – Space weather services that monitor the performance of global navigation satellite systems and warn users of possible disturbances are an important part of our modern infrastructure. Therefore, continuous efforts are made to improve these services (e.g., via post-event analyses). The present study gives an overview of the X-class solar flare during 9 February 2024 and presents an approach to complement total electron content maps for a better representation of the flare impacts. Furthermore, the specific energy absorption profile of the flare in the upper atmosphere is discussed, as well as the possibility to use the shape of the profile for assessing the flare impact on navigation and communication services.

1. Introduction

Post-event analyses of solar flares are an integral part of improving space weather services and products [1] and thus help to provide better information for users of global navigation satellite systems (GNSS). The impacts of solar flares on the ionosphere [2] and the resulting degradation of the GNSS positioning accuracy [3] are well studied, but a better description of spatial and temporal variations is crucial. The present study focuses especially on the limitations of total electron content (TEC) maps to describe such disturbances. For that purpose, the X3.38 solar flare during 9 February 2024 at 13:14 Coordinated Universal Time (UTC) is discussed for the observed solar spectrum, absorption in the atmosphere, and corresponding ionospheric response. The event is a suitable candidate for an investigation, as no geomagnetic activity (Kp ≤ 3) and therefore also no superposition of ionospheric enhancements occurred.

The results of the analysis are used to present an approach that complements the TEC maps and could provide GNSS users with essential information. This, in turn, could allow an improved awareness of natural (space weather) or artificial (e.g., jamming) degradation of the GNSS positioning accuracy [4, 5], as well as the distinction.

2. Data

Measurements of the extreme ultraviolet (EUV) and X-ray radiation are the main data sets to describe and classify solar flares. The Geostationary Operational Environmental Satellites of the R Series (GOES-R) measure solar bands with the EUV and X-Ray Sensors (EXIS) on board the satellites [6]. The GOES X-Ray Sensor (XRS) measures two bandpass channels from 0.05 nm to 0.4 nm and from 0.1 nm to 0.8 nm [7], which are used to classify solar flares according to the National Oceanic and Atmospheric Administration (NOAA) Space Weather Prediction Center (SWPC) scale. The GOES EUV measures seven solar emission lines and the Mg II core-to-wing ratio [8]. These measurements are provided in high temporal resolution, and 1 min averages are applied in the present study. The GOES-R EXIS data are available via the NOAA National Geophysical Data Center Web interface.

An overview of the whole solar spectrum is important to understand the ionospheric response during the solar flare event. For that reason, additional solar EUV and X-ray measurements are included in the present study. The Thermosphere Ionosphere Mesosphere Energetics and Dynamics (TIMED) satellite mission measures the solar irradiance with the Solar EUV Experiment (SEE) on board the satellite [9–11]. Two sensors, the Extreme-Ultraviolet Grating Spectrograph and the X-Ray-Ultraviolet Photometer System, measure the solar irradiance from 26 nm to 190 nm, from 0.1 nm to 35 nm, and at 121.5 nm [11]. The measurements are performed for approximately 3 min each 97 min orbit and are combined to a joined solar irradiance spectrum with intervals of 1 nm. The TIMED SEE data are available via the SEE Web page by the Laboratory for Atmospheric and Space Physics.

TEC maps generated at the Ionosphere Monitoring and Prediction Center (IMPC) of the German Aerospace Center are based on ground-based GNSS measurements that are assimilated into the Neustrelitz Total Electron Content Model (NTCM) [12]. The GNSS measurements of the International GNSS Service are acquired from different providers and applied to calculate $2.5^\circ \times 2.5^\circ$ TEC maps every 5 min in real time [13]. The data, including global and European near real-time TEC maps, are available via the IMPC Web page. The IMPC TEC maps are applied in the preceding studies to investigate extreme space weather events [1] and include various processing information (e.g., satellite–receiver configurations or NTCM results), allowing comprehensive analysis of the ionosphere during solar flares.

3. Solar Flare Event of 9 February 2024

Figure 1 shows the solar EUV and X-ray variations during the X3.38 flare on 9 February 2024 with GOES-16 measurements. The magnitude of the flare, according to the NOAA SWPC scale, is based on the peak of the XRS-B measurements at 13:14 UTC. The solar EUV irradiance

Manuscript received 17 October 2024.

Erik Schmölter and Jens Berdermann are with the German Aerospace Center, Institute for Solar-Terrestrial Physics, Kalkhorstweg 53, 17235 Neustrelitz, Germany; e-mail: Erik.Schmoelter@dlr.de, Jens.Berdermann@dlr.de.

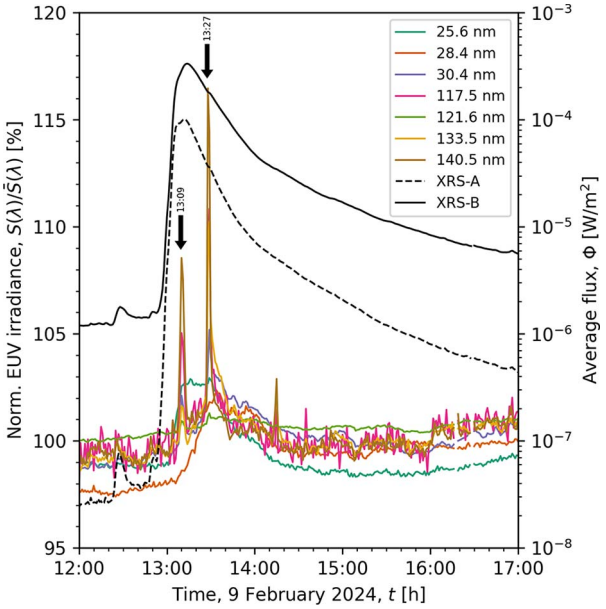

Figure 1. Solar EUV irradiance and average X-ray flux measured by the GOES-16 sensors during 9 February 2024 from 12:00 UTC to 17:00 UTC. The solar EUV irradiance is normalized by division with the daily mean of each spectral line. The arrows indicate the two major EUV peaks.

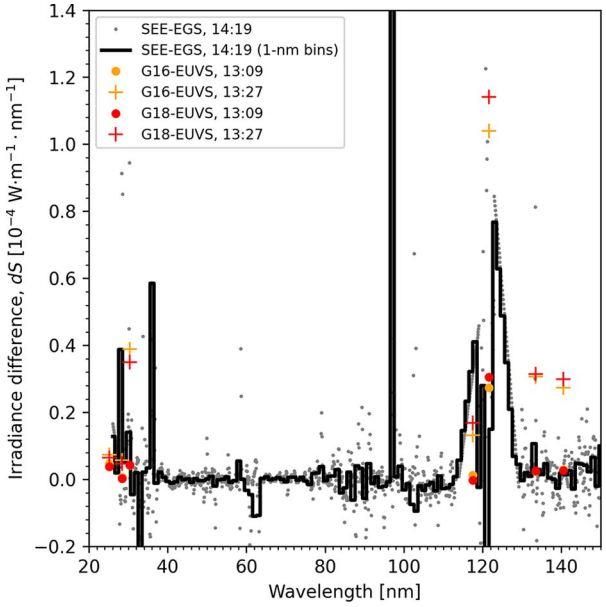

Figure. 2. Difference of the solar EUV irradiance during the solar flare on 9 February 2024 compared to nonflare conditions. The grey dots and black line (1 nm bins) show the difference for TIMED SEE measurements from 12:42 UTC to 14:19 UTC. The orange and red markers show the difference for GOES-16 and GOES-18 EUV measurements from 12:42 UTC to 13:09 UTC (dots) and 13:27 UTC (crosses). These times are selected based on the peaks in Figure 1.

shows distinct peaks at approximately 13:09 UTC and 13:27 UTC for different spectral lines. Such double peaks were also observed in previous studies with impacts on the ionosphere and applications during each enhancement [1]. For that reason, note the variations of the whole solar spectrum.

Figure 2 shows that the strongest EUV enhancement during both peaks occur for the spectral line of 121.6 nm. Smaller enhancements are observed for spectral lines of 30.4 nm, 117.5 nm, 133.5 nm, and 140.5 nm. Generally, the second increase of the solar irradiance is stronger at all spectral lines. The difference between GOES-16 and GOES-18 measurements is small, but GOES-16 differences are larger at spectral lines of shorter wavelength, and GOES-18 differences are larger at spectral lines of longer wavelength. Figure 2 shows also the measured difference of the EUV spectrum by TIMED SEE between the first measurement time before (12:42 UTC) and after (14:19 UTC) the flare. The 1 nm bins of this spectrum show an increase at shorter wavelengths (<40 nm) and around the Lyman alpha line (110 nm to 130 nm). Thus, enhancements of the solar spectrum are observed for an extended period of time and vary at different wavelengths.

4. Ionospheric Response

The observed changes in the solar spectrum during the solar flare increase the energy deposition q_f in the upper atmosphere, which, in turn, changes the plasma density. For the purpose of this study, q_f is estimated with the solar zenith angle χ, which, in turn, depends on longitude λ, latitude ϕ, and time t, according to

$$q_f(\lambda, \phi, t) \simeq I_f(t) \cdot e^{-\sec \chi(\lambda,\phi,t)} \quad (1)$$

The solar irradiance I_f only works as a scaling factor during a specific time (peak time for flare), and the second term includes the spatial variability. For the analysis of the ionospheric response, the wavelength- and altitude-dependent absorption processes must be included too. For that purpose, an absorption profile for a dayside ionosphere [14] with all regions is modeled according to

$$q(h) = \sum_{\lambda} \sum_{i} n_i(h) \cdot \sigma_i(\lambda) \cdot I(h) \quad (2)$$

The total absorption cross sections σ for N_2, O, and O_2 are retrieved from various sources [15–17]. The altitude-dependent irradiance I is calculated with (1) for the dayside center location by setting χ to 0°. The density profiles n of N_2, O, and O_2 are retrieved from the empirical, global reference atmosphere model NRLMSISE-00 [18].

The ratio of the calculated absorption is shown in Figure 3, which reflects the amount of the initial solar flux that is absorbed at each altitude. The result shows distinct features at different wavelength and altitudes. The ionospheric F layer is created dominantly via the ionization of O (but also N_2), which occurs at wavelength from 5 nm to 90 nm. Thus, the increased EUV radiation during the solar

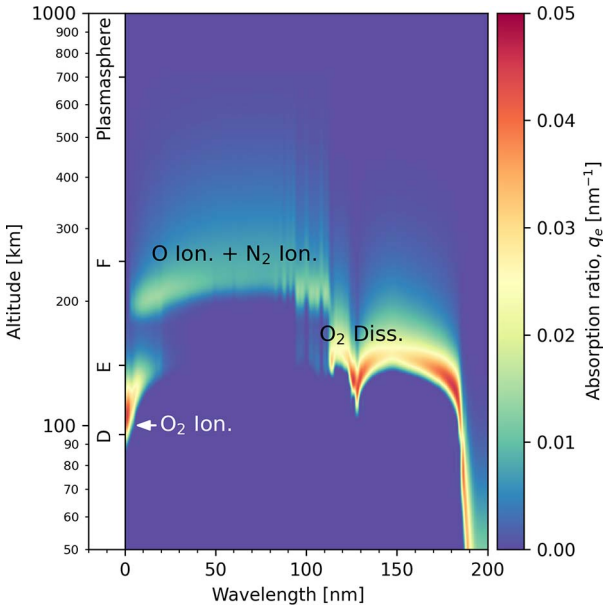

Figure 3. The major absorption processes including ionization (Ion.) and dissociation (Diss.) for N_2, O, and O_2 are shown for the ionosphere at the dayside center location. The absorption ratio describes the amount of the initial solar flux that is absorbed at each altitude. The ionospheric layers are assigned to altitudes with distinct absorption processes.

flare event (see Figure 1) is expected to affect the F layer up to the topside ionosphere. At a wavelength shorter than 25 nm, the absorption is dominated by ionization of O_2 in the D and E layer. Especially strong ionization occurs at a wavelength shorter than 5 nm in the D layer. Thus, the increased X-ray radiation during the solar flare event (see Figure 1) is expected to cause significant enhancements within this layer. Dissociation processes at a wavelength longer than 100 nm may also be enhanced (see Figure 2) but are less important for disturbances of the plasma density.

The various solar flare-driven processes were discussed with comprehensive ionosphere models [2], but the results in Figure 3 highlight the processes that may occur due to the various EUV and X-ray peaks (see Figure 1) of the investigated event. This insight is crucial to understand the temporal and spatial changes of the TEC response.

Figure 4 shows the TEC rate after the main solar flare peak at 13:20 UTC. The TEC rate in the European region stands out with a significant increase. This stronger flare impact at mid compared with low latitudes may be expected, because TEC is generally lower and thus more susceptible to enhancements. However, the region also covers the impact better, as the amount of TEC measurements is significantly higher due to the dense GNSS receiver network (approximately three times more measurements then all other dayside areas combined). It is, therefore, possible that an impact in other regions (i.e., subsolar region) is not identified due to the low number of measurements. For that reason, the ratio of the preflare TEC and estimated energy

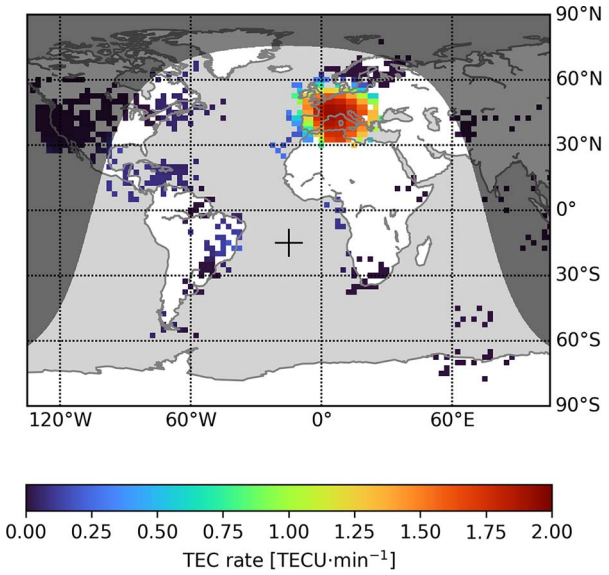

Figure 4. The TEC rate during the X3.38 solar flare on 9 February 2024 at 13:20 UTC. The shading indicates the nightside. The cross marks the geographical position where the solar zenith angle is 0°.

deposition $q_f(1)$ is calculated to estimate where the ionosphere is susceptible to interactions with the solar flare. Figure 5 shows $\frac{q_f}{\mathrm{TEC}}$ for the 9 February 2024 X3.38 solar flare. The global structure on the dayside is reflecting q_f, but small-scale features are visible due to TEC. The regions with low density of GNSS receivers are better represented. Thus, this information could be provided for GNSS users

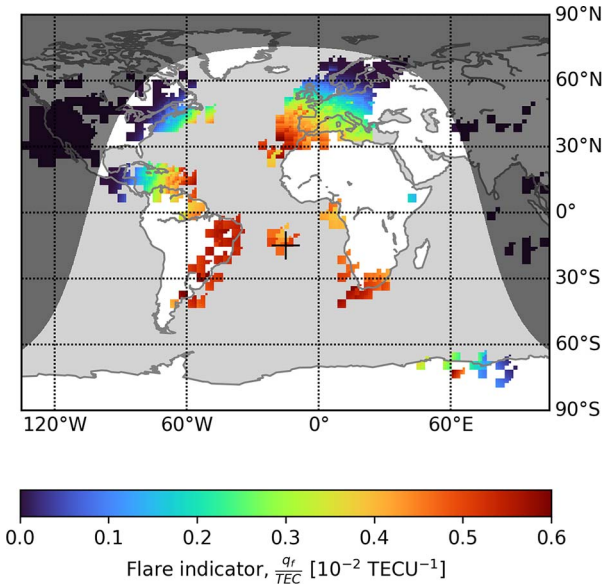

Figure 5. Indicator for probability of ionospheric interactions during the solar flare on 9 February 2024 at 13:20 UTC. The shading indicates the nightside. The cross marks the geographical position where the solar zenith angle is 0°.

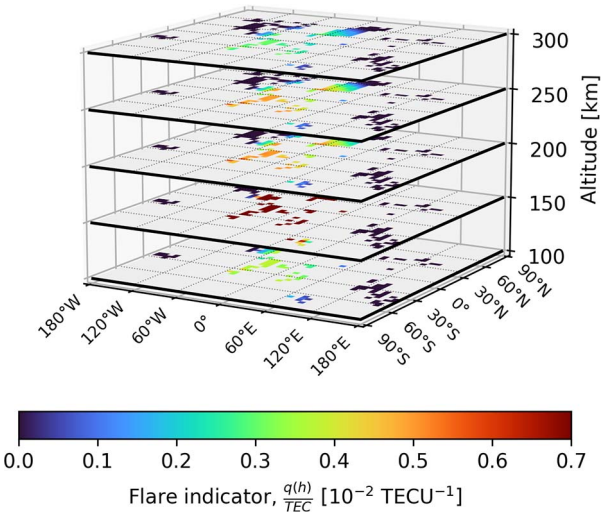

Figure 6. Indicator for probability of ionospheric interactions at selected altitudes during the X3.38 solar flare on 9 February 2024 at 13:20 UTC.

to warn of possible disturbances that are not captured with TEC maps.

The approach is also applied at different altitudes using $q(h)$. The resulting flare indicator $\frac{q(h)}{\mathrm{TEC}}$ is shown for selected altitudes in Figure 6. A significantly stronger response occurs at altitudes below 120 km due to ionization of O_2 (see Figure 3). The spatial variations are differently affected at each altitude, resulting in a unique profile for the solar flare. This result is of particular interest for future studies, as solar flares with different X-ray and EUV components could be analyzed for distinct altitude-dependent profiles. This, in turn, could help to further define the extent of ionospheric disturbances in near real-time TEC.

5. Conclusion

Post-event analyses are important to improve space weather services and may lead to new or improved products. The present study provided insights into a single solar flare event and showed that the successful detection of disturbances in the ionosphere depends on a dense network of GNSS receivers. It is shown that an indicator taking into account the additional absorption of the solar flare's energy in the undisturbed ionosphere can supplement TEC maps with valuable additional information and issue better support for providers of various communication and navigation services (see Figure 5). Future analyses can examine in detail whether the approach can also be successfully applied to other flare events. Because each flare has a specific energy spectrum and a related absorption profile in the upper atmosphere, it is possible to define different flare profile classes and the impact on communication and navigation services. This information could be archived for each past solar flare event, which would allow a comparison with new flares as soon as the energy spectrum is known. This, in turn, would allow providing ad hoc information about impacts, which were observed for similar flares in the past and are likely to occur for the new event.

6. Acknowledgments

The authors thank NOAA and LASP for making solar observations publicly available. The GOES-R data were obtained from the NOAA GOES-R Space Weather (https://www.ngdc.noaa.gov/stp/satellite/goes-r.html). The TIMED SEE data were obtained from the Laboratory for Atmospheric and Space Physics (https://lasp.colorado.edu/home/see/data/). The German Aerospace Center total electron content maps were obtained from the IMPC (https://impc.dlr.de).

7. References

1. J. Berdermann, M. Kriegel, D. Banyś, F. Heymann, M. M. Hoque, et al., "Ionospheric Response to the X9.3 Flare on 6 September 2017 and Its Implication for Navigation Services Over Europe," *Space Weather*, **16**, 10, October 2018, pp. 1604-1615.
2. L. Qian, A. G. Burns, P. C. Chamberlin, and S. C. Solomon, "Variability of Thermosphere and Ionosphere Responses to Solar Flares," *Journal of Geophysical Research: Space Physics*, **116**, A10, October 2011, pp. 1-14.
3. Y. Yasyukevich, E. Astafyeva, A. Padokhin, V. Ivanova, S. Syrovatskii, et al., "The 6 September 2017 X-Class Solar Flares and Their Impacts on the Ionosphere, GNSS, and HF Radio Wave Propagation," *Space Weather*, **16**, 8, July 2018, pp. 1013-1027.
4. V. Sreeja, "Impact and mitigation of space weather effects on GNSS receiver performance," *Geoscience Letters*, **3**, 24, August 2016, pp. 1-13.
5. M. Cuntz, A. Konovaltsev, A. Dreher, and M. Meurer, "Jamming and Spoofing in GPS/GNSS Based Applications and Services—Threats and Countermeasures," 7th Security Research Conference, Bonn, Germany, September 4-6 2012, pp. 196–199.
6. J. L. Machol, F. G. Eparvier, R. A. Viereck, D. L. Woodraska, M. Snow, et al., "GOES-R Series Solar X-ray and Ultraviolet Irradiance," in S. J. Goodman, T. J. Schmit, J. Daniels, and R. J. Redmon (eds.), *The GOES-R Series*, Amsterdam, Elsevier, 2020, Chapter 19.
7. P. Chamberlin, T. Woods, F. Eparvier, and A. Jones, "Next Generation X-Ray Sensor (XRS) for the NOAA GOES-R Satellite Series," SPIE Optical Engineering + Applications, San Diego, California, United States, August 2-6 2009, pp. 743802-1-743802-10.
8. F. G. Eparvier, D. Crotser, A. R. Jones, W. E. McClintock, M. Snow, et al., "The Extreme Ultraviolet Sensor (EUVS) for GOES-R," SPIE Optical Engineering + Applications, San Diego, California, United States, August 2-6 2009, pp. 743804-1-743804-8.
9. T. N. Woods, S. M. Bailey, F. G. Eparvier, G. M. Lawrence, J. Lean, et al., "TIMED Solar EUV Experiment," SPIE's International Symposium on Optical Science, Engineering, and Instrumentation, San Diego, California, United States, July 19-24 1998, pp. 180–191.
10. T. N. Woods, S. Bailey, F. Eparvier, G. Lawrence, J. Lean, et al., "TIMED Solar EUV Experiment," *Physics*

and Chemistry of the Earth, Part C: Solar, Terrestrial & Planetary Science, **25,** 5–6, March 2000, pp. 393-396.
11. T. N. Woods, "Solar EUV Experiment (SEE): Mission Overview and First Results," *Journal of Geophysical Research*, **110**, A1, January 2005, pp. 1-24.
12. N. Jakowski, C. Mayer, M. M. Hoque, and V. Wilken, "Total Electron Content Models and Their Use in Ionosphere Monitoring," *Radio Science*, **46**, 6, September 2011, pp. 1-11.
13. M. Kriegel and J. Berdermann, "Ionosphere Monitoring and Prediction Center," 2020 European Navigation Conference, Dresden, Germany, November 23-24 2020, pp. 1-10.
14. G. W. Prölss, *Physik des erdnahen Weltraums*, Berlin, Springer, 2004.
15. R. Ladenburg and C. C. Van Voorhis, "The Continuous Absorption of Oxygen Between 1750 and 1300A and Its Bearing Upon the Dispersion," *Physical Review*, **43**, 5, March 1993, pp. 315-321.
16. R. D. Hudson and S. H. Mahle, "Photodissociation Rates of Molecular Oxygen in the Mesosphere and Lower Thermosphere," *Journal of Geophysical Research*, **77**, 16, June 1972, pp. 2902-2914.
17. J. A. Fennelly and D. G. Torr, "Photoionization and Photoabsorption Cross Sections of O, N2, O2, and N for aeronomic calculations," *Atomic Data and Nuclear Data Tables*, **51**, 2, July 1992, pp. 321-363.
18. J. M. Picone, A. E. Hedin, D. P. Drob, and A. C. Aikin, "NRLMSISE-00 Empirical Model of the Atmosphere: Statistical Comparisons and Scientific Issues," *Journal of Geophysical Research: Space Physics*, **107**, A12, December 2002, pp. SIA 15-1-SIA 15-16.